International Forum on Aeroelasticity and Structural Dynamics
IFASD 2019
9-13 June 2019, Savannah, Georgia, USA

SURROGATE-BASED OPTIMIZATION OF A MORPHING WINGLET FOR FLEXIBLE AIRCRAFT

Martin Delavenne[2,1], Bernard Barriety[1], Fabio Vetrano[1], Valerie Ferrand[2], Michel Salaun[2]

[1]Airbus Operations SAS
316 route de Bayonne, Toulouse, France
martin.m.delavenne@airbus.com

[2]ISAE-SUPAERO
Universite de Toulouse, France
valerie.ferrand@isae-supaero.fr
michel.salaun@isae-supaero.fr

Keywords: Active Winglet, Static Aeroelasticity, Multidisciplinary-optimization, CFD/CSM, Surrogate-models.

Abstract: Since the pioneering work by Whitcomb [1] in the mid-70's winglets have demonstrated their capabilities to improve aircraft efficiency. However, they are fixed devices and optimized for certain flight conditions. This paper investigates the opportunity to make these wing extensions active to control aircraft performances along the flight. To assess the efficiency of such a technology, high-fidelity computations coupling aerodynamics and structural mechanics disciplines are used. Surrogate models are built to speed-up the optimization process. Multi-objective and gradient-free algorithms are used to search the optimal winglet shape in cruise condition and the optimal winglet deflection along the mission with block fuel minimization as objective. The capability of active winglets to control the wing shape and particularly the twist is demonstrated. It is also highlighted that the wing flexibility is a key driver of the efficiency of active winglets and must be considered to assess the performances of morphing devices. This document shows that depending on the baseline choice the gains can be quadrupled if the stiffness is neglected.

1 INTRODUCTION

Since the very beginning of aviation history aircraft manufacturers have been stretching their imagination to propose the most efficient products and particularly to reduce fuel consumption. In recent years, this preoccupation has been center stage with combination of oil prices increase and expansion of global warming. Much efforts were concentrated on the optimization of the wing-tube configuration: profile shapes were designed to reduce drastically wave and viscous drag, engines performances were dramatically improved and every aircraft were equipped with wing-tips designed to decrease the induced drag. However, this configuration is reaching its limits and a new paradigm must be considered. Quite recently, Boeing introduced the folding wing-tip that aims to increase the wing span once in the air and so reducing the drag while still be compliant with airport regulation once on ground [2]. This is the first step toward more versatile aircraft configurations. Nevertheless, this step-forward still relies on the 'old' process that consists in the optimization of the aircraft for a limited number of flight conditions.

The future is to fully adaptive configurations optimized for each point of the flight domain. Morphing technologies are promising solutions that become popular among the aeronautic community and many studies are dedicated to the subject [3, 4]. Morphing, i.e. changing aircraft form depending on the flight conditions, is not new in aviation history since the very first plane, the Wright Flyer, had taken-off with differential wrapping wings for rolling control. Then flaps and slats were introduced to improve the landing characteristics as aircraft were gaining speed. Even the flapping nose of the Concorde may be consider as a morphing device dedicated to improve the pilots' visibility. However these devices were designed to act on a narrow range of flight conditions. Today studies on morphing devices focus on technologies that enable to control (mainly) the wing shape all along the flight. Most of them deal with trailing edge devices, that represent the most promising solutions as they enable to reduce drag, noise but also loads and may even be used for flutter control. All these considerations may lead to block fuel saving up to 10% [5–9]. However, the actuation system of such devices may have a detrimental weight and is still one of the blocking point to be solved before implementation on civil aircraft. The certification is also an issue that must be tackled [10].
Active winglet concept is at the crossing between wing morphing technologies and folding wing-tips. The technology studied in this paper is inspired by the concept patented by Airbus in the early 2000's [11]. This device takes advantage of the span increase due to the folding wing-tip but is also thought to be able to optimize the aircraft performances along the flight by acting on the wing shape. Previous conceptual studies on similar concepts and using intermediate-fidelity tools estimated that additional 2% of block fuel can be saved comparing to fixed winglet configurations [12, 13]. The present analysis aims to assess the capability of active winglets to efficiently control aircraft performances during a flight. High-fidelity CFD/CSM (Computational Fluid Dynamics/ Computational Structural Mechanics) are used to properly evaluate the aerodynamic performances and the wing displacements. Engine performances are also considered to have to estimate precisely the fuel burnt. XRF1 model, an Airbus provided industrial standard multi-disciplinary research test-case representing a typical configuration for a long range wide body aircraft, is considered. A winglet is optimized for this configuration at the design point using surrogate models and multi-objectives algorithm. The cant angle of this design is then adjusted for all points of a typical mission to minimize the fuel burnt using a gradient-free differential evolution algorithm. Computations with rigid and flexible wings are performed to highlight the sensitivity of the winglet efficiency with respect to the wing stiffness.

2 THEORETICAL BACKGROUND OF SURROGATE-BASED OPTIMIZATION

2.1 Design of Experiment

For every problem dealing with surrogate models the first stage consists in the selection of the sampling points. Indeed, these models aim to approximate an expensive (computationally or experimentally) or difficult to evaluate (experiment data) function, based on the observations at a limited and predefined number of points. The selection of these points, called the sampling plan or the Design of Experiment (DoE), is determinant as the accuracy of the models highly depends on their spreading and their number.
Let's N be the dimension of design space and assume that each direction can be split in n levels, it forms a partition of the design space into n^N 'boxes'. A first DoE consists in filling each box with a randomly selected sample. This is called a *Full Factorial* sampling plan. It has the advantage of being uniform i.e same number of points in each direction. However, the number of calls to the expensive function is n^N and may rapidly becomes detrimental for high dimension problems and/or high accuracy requirements. There is a need for smarter techniques to reduce the number of samples, one of the most popular is the Latin Hypercube Sampling

(LHS). The design space is still divided into n^N boxes, here the objective is not to fill all the boxes but to have each level of a direction filled with exactly one point as illustrated on Figure 1. This sampling technique ensures a projected uniformity in each direction and requires only

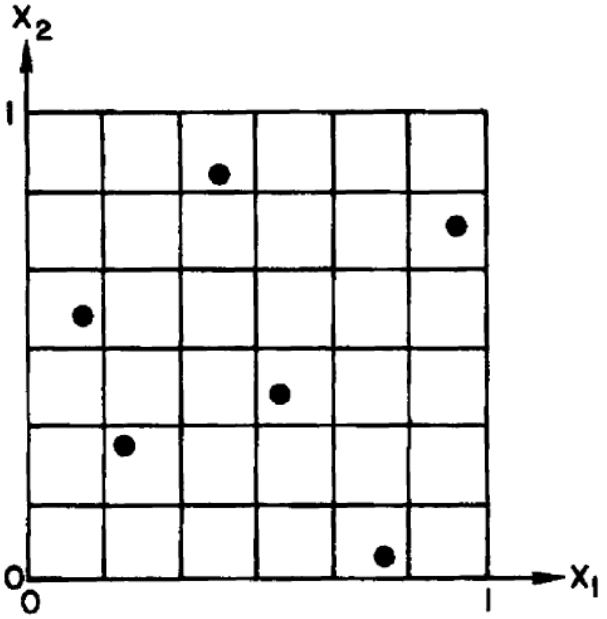

Figure 1: Example of Latin HyperCube Sampling for N=2 and n=6, from [14]

n evaluations of the expensive function. However, for each level points being quasi-randomly selected, the global uniformity is not guaranteed with possible consequence on the quality of the surrogate model. Indeed, the first sample is selected randomly in a box of the design space that is also randomly selected, then all the boxes on the same levels as the selected one are remove from the set of boxes. A second box is randomly chosen in the remaining ones and a sample is randomly picked in this box, the schema is iterate until their is no remaining boxes. Solutions exist to improve the global uniformity of LHS: the minimal distance between samples can be maximized, the correlation between samples can be minimized or the DoE can be optimized using a Stochastic Evolutionary Algorithm [15]. This latter option was selected in our study to improve the spreading of the sampling points. This methods has the advantage to use a global search technique that guarantee to find a solution near to the global optimum and to be compatible with several quality criteria such as maximum minimal distance. Given an optimal sampling plan matrix $\boldsymbol{X} = [\boldsymbol{x}^{(1)}, ..., \boldsymbol{x}^{(n)}]$ of n configurations $\boldsymbol{x}^{(i)}$ the output vector from the expensive function can be derived $\boldsymbol{y} = (y^{(1)}, ..., y^{(n)})$, the set $\left\{(\boldsymbol{x}^{(1)}, y^{(1)}), ..., (\boldsymbol{x}^{(n)}, y^{(n)})\right\}$ forms the learning data-base.

2.2 Surrogate modelling

In many engineering problems as soon as high-fidelity is targeted the limiting factor is the computational time/cost. This could make some simulations not suitable for optimization purposes. To cope with this issue, a solution is to approximate the "true" functions f, in our case CFD/CSM simulations results, by simplified and cheap-to-evaluate mathematical models $\hat{f}$. Many kind of techniques exist among the most popular we can cite:

- Polynomial regressions
- Radial basis function models
- Gaussian process / Kriging models

The objective of the surrogate model building is to find the parameters of the models that best fit the observed data $\boldsymbol{y}$. The principles of the three above-mentioned models will be detailed in the next sub-paragraphs.

2.2.1 Polynomial regressions

The simplest way to introduce polynomial models is to consider a one dimension problem. Let's take the example of a degree m function to approximate f:

$$\hat{f}(x) = \omega_0 + \sum_{j=1}^{m} \omega_j x^j \tag{1}$$

The parameters ω are selected to minimize the squared error with respect to the data-base points:

$$\min_{\omega} \sum_{i=1}^{n} (y^{(i)} - \hat{f}(x^{(i)}))^2 \tag{2}$$

Polynomial models are regressive and are suited if the function to model is thought to be polynomial, otherwise the approximation error could be high. In the frame of optimization problem that means that some optimum may not be captured. Besides, the higher the degree the more flexible the model i.e. the model will be able to limit the error at the sampling points but the higher risk to over fit the data and to introduce artificial noise. To finish, the example deals with a simple 1D case, if more dimensions are to be considered the formulations becomes more complex with interaction terms:

$$\hat{f}(\boldsymbol{x}) = \sum_{j=1}^{M} \omega_j \Psi_i(\boldsymbol{x}) \tag{3}$$

Where Ψ_i are functions taken from the set of all functions of order m or lower. To find the $\omega' s$ parameters and choose the Ψ functions to be used becomes a fastidious task.

2.2.2 Radial basis function models

Radial basis functions (RBF) are classes of interpolating functions whose values depends on the distance from center points. In the frame of surrogate modelling it is wise to use the sampling points as centers. The formulation of the substitution function becomes:

$$\hat{f}(\boldsymbol{x}) = \sum_{j=1}^{n} \omega_i \psi(||\boldsymbol{x} - \boldsymbol{x}^{(j)}||) \tag{4}$$

Radial basis functions ψ can be chosen among non-parametric forms, whose most popular are:

1. Linear function $\psi(r) = r$
2. Cubic function $\psi(r) = r^3$
3. Thin plane spline $\psi(r) = r^2 \log(r)$

In the present case only $\omega' s$ parameters must be found, this is done considering the interpolating properties of the model at each sampling points:

$$y^{(i)} = \sum_{j=1}^{n} \omega_j \psi(||\boldsymbol{x}^{(i)} - \boldsymbol{x}^{(j)}||) \tag{5}$$

This can be sum up by the linear system:

$$\boldsymbol{y} = \boldsymbol{\omega}\boldsymbol{\psi} \tag{6}$$

More complex parametric functions that enable more flexibility can also be chosen:

1. Multi-quadratic $\psi(r) = \sqrt{r^2 + \gamma^2}$
2. Gaussian $\psi(r) = \exp\left(\frac{-r^2}{2\sigma^2}\right)$

The parameters γ or σ are fixed by minimization of the cross-validation error. This method consist in removing a test set of n_s points from the DoE, fit a model for the remaining $n - n_s$ points and test the model on the test set. Errors can be derived, for example the Mean Squared Error(MSE):

$$MSE = \frac{\sum_{j=1}^{n_s}(y^{(j)} - \hat{f}(\boldsymbol{x}^{(j)}))^2}{n_s} \tag{7}$$

The operation can be reproduced for several test sets, the cross-validation error being the mean value of the errors. A limit case is when the number of test sets equal the number of sampling points and $n_s = 1$, this is called the leave-on-out cross-validation. The parameter that presents the lowest cross-validation error is selected. Note that for each parameter the $\omega' s$ must be recomputed using (6).

2.2.3 Kriging and Gaussian processes

An other class of surrogate models that is widely used is Kriging also known and generalized as Gaussian Processes (GP). This kind of models relies on the work by the geophysicist Danie Krige in the 50's [16]. Here an output from the expensive function can be seen as the results of a random process $Y(\boldsymbol{x})$ following a normal law $\mathcal{N}(\mu, \sigma)$. For two points in the design space $\boldsymbol{x}^{(i)}$ and $\boldsymbol{x}^{(j)}$, the outputs are then random variables correlated with each other according to the following formula:

$$Corr(Y(\boldsymbol{x}^i), Y(\boldsymbol{x}^j)) = \exp(-\sum_{k=1}^{N} \theta_k |x_k^{(i)} - x_k^{(j)}|^{p_k}) \tag{8}$$

In (8) N is the dimension of the design space θ_k and p_k are hyperparameters of the model that are determined such that the model goes through the database points. The hyperparameters represent respectively the influence on the output of a given direction in the design space and the smoothness of the output in this direction. In other words a high θ_k means the direction k will have significant influence and a high p_k means that the output will vary smoothly in the direction k. Considering the sampling points $\boldsymbol{X}$ and their responses $\boldsymbol{y}$, a correlation matrix $\boldsymbol{C}$ can be derived:

$$\boldsymbol{C} = \begin{bmatrix} Corr(Y(\boldsymbol{x}^{(1)}), Y(\boldsymbol{x}^{(1)})) & ... & Corr(Y(\boldsymbol{x}^{(1)}), Y(\boldsymbol{x}^{(n)})) \\ Corr(Y(\boldsymbol{x}^{(2)}), Y(\boldsymbol{x}^{(1)})) & ... & Corr(Y(\boldsymbol{x}^{(2)}), Y(\boldsymbol{x}^{(n)})) \\ \vdots & ... & \vdots \\ Corr(Y(\boldsymbol{x}^{(n)}), Y(\boldsymbol{x}^{(1)})) & ... & Corr(Y(\boldsymbol{x}^{(n)}), Y(\boldsymbol{x}^{(n)})) \end{bmatrix} \tag{9}$$

The parameters μ, σ, $\theta' s$ and $p' s$ are estimated by maximization of the likelihood function for the database points:

$$L = \frac{1}{(2\pi\sigma^2)^{\frac{n}{2}}|\boldsymbol{C}|^{0.5}} \exp\left(\frac{-(\boldsymbol{y} - \boldsymbol{\mu})\boldsymbol{C}^{-1}(\boldsymbol{y} - \boldsymbol{\mu})}{2\sigma^2}\right) \tag{10}$$

This function represents the probability for a given set of parameters to represent correctly the observed data of the sampling plan. Taken the logarithm of expression (10) without constant terms:

$$\ln(L) \approx -\frac{n}{2}\ln\left(\sigma^2\right) - 0.5\ln\left(|\boldsymbol{C}|\right) - \left(\frac{-(\boldsymbol{y}-\boldsymbol{\mu})\boldsymbol{C^{-1}}(\boldsymbol{y}-\boldsymbol{\mu})}{2\sigma^2}\right) \tag{11}$$

Looking for an extremum the derivatives with respect to σ and μ should be null which leads to:

$$\mu = \frac{\boldsymbol{I^t C^{-1} y}}{\boldsymbol{I^t C^{-1} I}} \tag{12}$$

$$\sigma = \frac{(\boldsymbol{y}-\boldsymbol{\mu})\boldsymbol{C^{-1}}(\boldsymbol{y}-\boldsymbol{\mu})}{n} \tag{13}$$

In (12) $\boldsymbol{I}$ stands for the identity vector. Substituting (12) and (13) in (11) a formulation of the log-likelihood depending only on $\boldsymbol{C}$ i.e. on $\theta's$ and $p's$ parameters can be derived:

$$\ln(L) \approx -0.5n\ln\left(\sigma^2\right) - 0.5\ln(|\boldsymbol{C}|) \tag{14}$$

Once the parameters of the model are tuned the value at a new location $\boldsymbol{x}$ in the design space can be predicted by the following formula:

$$\hat{f}(\boldsymbol{x}) = \mu + C^t\boldsymbol{C^{-1}}(\boldsymbol{y}-\mu) \tag{15}$$

C is the correlation vector of the random variables $Y(\boldsymbol{x})$ at the new point and $Y(\boldsymbol{x}^{(i)})$ at sampling locations:

$$C = \begin{bmatrix} Corr(Y(\boldsymbol{x}), Y(\boldsymbol{x}^{(1)})) \\ Corr(Y(\boldsymbol{x}), Y(\boldsymbol{x}^{(2)})) \\ \vdots \\ Corr(Y(\boldsymbol{x}), Y(\boldsymbol{x}^{(n)})) \end{bmatrix} \tag{16}$$

Formula (15) is derived from the maximization of the augmented likelihood. Indeed, combining C and $\boldsymbol{C}$ a augmented correlation matrix can be constructed $\tilde{\boldsymbol{C}}$. In the same way, an augmented output vector $\tilde{\boldsymbol{y}} = [\boldsymbol{y}, \hat{f}(\boldsymbol{x})]$ is built. The log-likelihood function (11) is modified replacing $\boldsymbol{C}$ and $\boldsymbol{y}$ by their augmented counter-parts and using the method of Theil to compute the inverse of $\tilde{\boldsymbol{C}}$ as described in [17]. The derivative of the augmented log-likelihood with respect to $\hat{f}$ is computed and set to 0:

$$0 = (\hat{f}-\mu)\Big[\frac{-1}{\sigma^2(1-C^t\boldsymbol{C}^{-1}C)}\Big] + \Big[\frac{C^t\boldsymbol{C}^{-1}(\boldsymbol{y}-\boldsymbol{I}\mu)}{\sigma^2(1-C^t\boldsymbol{C}^{-1}C)}\Big] \tag{17}$$

Reorganizing (17) and using (13) leads to (15).

2.3 Surrogate-based optimization

2.3.1 Principle

This section is partly inspired by the reference article by Jones, [18]. In this paper, the author details the advantages and the drawbacks of different class of surrogate models for optimization purposes and particularly for finding the global optimum. The classical work-flow of the surrogate-based optimization is presented on Figure 2:

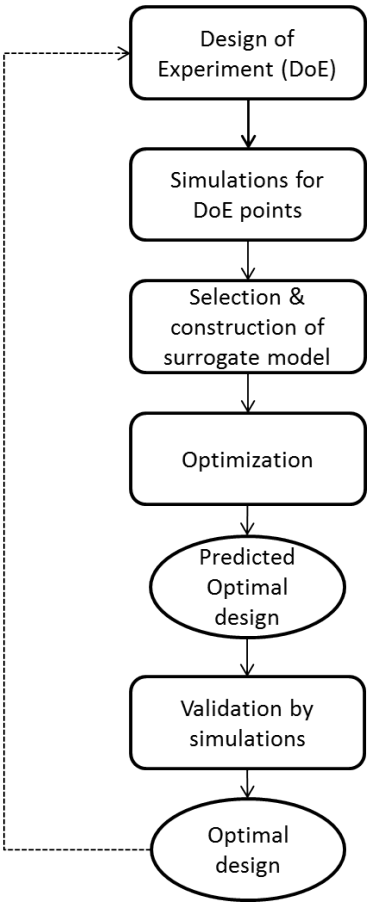

Figure 2: Surrogate-based optimization general work-flow.

As already detailed in the previous paragraph a DoE is first created, then the expensive function is evaluated for the sampling points, the surrogate is built and then exploited to find the optimum. This optimum must be validated with respect to the expensive function and added to the initial DoE. This process is iterated until convergence, i.e. the difference between two consecutive optimal designs is sufficiently small. In his paper, Jones shows that regressive models may be insensitive to the addition of new points in the database. Therefore, if the optimum is not well captured by the model there is very few chance that the addition of the ”true” value at that point will change drastically the results and the optimization will converged in very few iterations to inexact optimal design. Figure 3 shows how a polynomial regression model can fail to find the global optimum of a function.

Concerning Radial Basis Functions, Jones demonstrates that as soon as a local minimum is found, there is no further improvement expected. Indeed, as RBF are interpolating models adding a sampling point improves, locally, the prediction. But if the minimum is in the neighbourhood of a local optimal of the true function, as illustrated on Figure 4, adding the true local optimum in the database will slightly modify the model in this region, therefore the convergence will be reached quickly without capturing the global optimum. Therefore, RBF are suited to capture local optimum with great fidelity but there is no guarantee to find the global optimum. Besides, it is shown that if, very unlikely, the RBF is minimized at a sampling points no improvement is to be expected and the method is trapped on a point that may not be a global nor a local optimum. To cope with this issue it is recommended to force the model gradient to match with the ”true” function gradient by probing points in the vicinity of the predicted optimum and adding them to the database. However, Jones shows that even this method can fail to find the

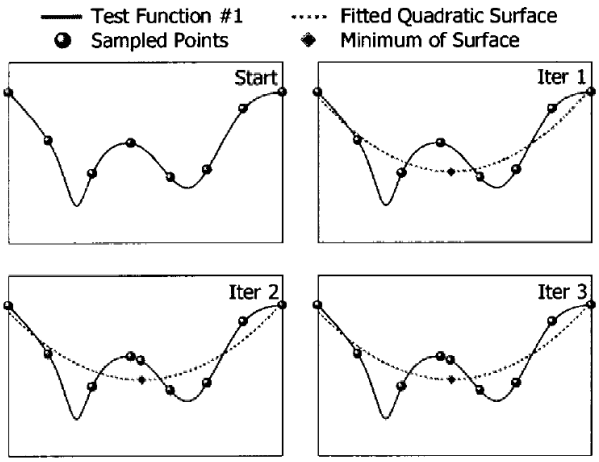

Figure 3: How polynomial regression can fail to find an optimum. From [18]

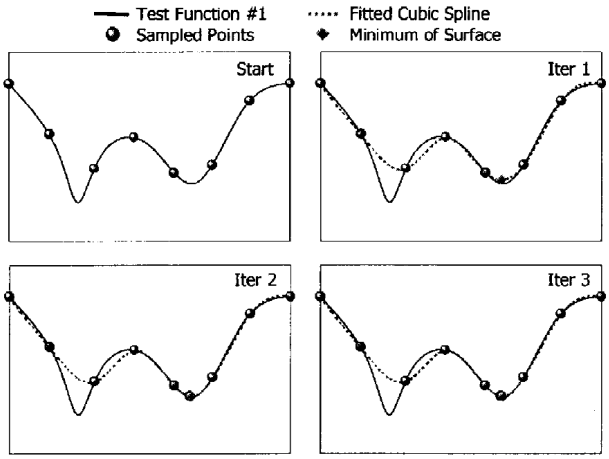

Figure 4: Illustration of surrogate-based optimization using RBF, here a local optimum is captured. From [18]

global optimum.

As explained above, surrogate-based optimization methods using polynomial and RBF may fail to find the global optimum because they only exploit the model i.e. they add new sampling points only in regions near an optimum of the model without taking into account areas of the design space that are less densely populated with sampling points and where an global optimum may be hidden. Therefore, to increase the probability to find the global optimum, methods that also explore the model should be used. It means that points should be added not only in regions near the optimum but also in areas where the uncertainty in the model is high. Therefore, we need to be able to quantify this uncertainty in the model. As explained in the previous paragraph, the prediction at a new point is computed by maximization of the likelihood at that point. If the sensitivity of the likelihood to the value of $\hat{f}$ in that region is quite low the uncertainty of the prediction will be high: another value of $\hat{f}$ slightly different will give almost the same likelihood value. On the contrary if the sensitivity is high, that is if the likelihood drops rapidly for different values of $\hat{f}$ in the vicinity of the best prediction, the confidence in that value will be higher. Therefore, to estimate the uncertainty in the model we need not only the maximum of likelihood i.e. the first derivative but also its double derivative with respect to $\hat{f}$. Taking (17), differentiating and inverting to retrieve a minimization problem:

$$Error \approx \sigma^2(1 - C^t \boldsymbol{C} C) \tag{18}$$

In [17, 18] it is shown that (18) can be augmented with an additional term to retrieve the Mean Square error of the Kriging prediction denoted s:

$$s^2(\boldsymbol{x}) = \sigma^2\big[(1 - C^t\boldsymbol{C}C) + \frac{(1 - C^t\boldsymbol{C}^{-1}C)^2}{\boldsymbol{I}^t\boldsymbol{C}^{-1}\boldsymbol{I}}\big] \tag{19}$$

This error estimation can be used to computed an "Expected Improvement" that is the expectation that the prediction at a new point $\boldsymbol{x}$ will improve the current optimum of the model $\hat{f}_{opt}$. Let I be the amount of improvement, $Y(\boldsymbol{x})$ the random variable representing the value of the output at the location $\boldsymbol{x}$. Y is normally distributed around $\hat{f}(\boldsymbol{x})$ and the standard deviation is $s^2(\boldsymbol{x})$. The Expected Improvement (EI) is expressed as the expectation of the likelihood of having the improvement I at $\boldsymbol{x}$:

$$E(I) = (\hat{f}_{opt} - \hat{f}(\boldsymbol{x}))\Phi\Big(\frac{\hat{f}_{opt} - \hat{f}(\boldsymbol{x})}{s(\boldsymbol{x})}\Big) + s(\boldsymbol{x})\phi\Big(\frac{\hat{f}_{opt} - \hat{f}(\boldsymbol{x})}{s(\boldsymbol{x})}\Big) \tag{20}$$

In (20) $\Phi(X)$ and $\phi(X)$ are respectively the the cumulative distribution and the density functions of the normal law. In the frame of the optimization based on Kriging models and using the EI, the objective function $\hat{f}$ to be minimized is replaced by the maximization of the EI. According to (20), it has the advantage to balance the exploitation of the model ($\Phi\Big(\frac{\hat{f}_{opt} - \hat{f}(\boldsymbol{x})}{s(\boldsymbol{x})}\Big)$ term) and the exploration of regions with high uncertainty ($s(\boldsymbol{x})\phi\Big(\frac{\hat{f}_{opt} - \hat{f}(\boldsymbol{x})}{s(\boldsymbol{x})}\Big)$ term).
The principle of the optimization based on expected improvement maximization is illustrated on Figure 5, for this illustrative problem the test function $(6x - 2)^2 \sin(12x - 4)$ is minimized. This wise selection of the additional sampling points is a key characteristics of Gaussian processes and make them particularly attractive to find the global optimum. For these reasons, in this work it was decided to use this class of models to perform the optimization of the winglet geometry and of the mission performances.

2.3.2 Search the surrogate models

Whatever the method used, there is a need to search directly the model or an associated function, in the case of "Expected Improvement" for example. In this study, surrogate models are used to perform both single and multiple objectives optimization to minimize both the drag and the impact on structure.
For single objective optimization the surrogate model or the associated function can be search by a gradient free optimizer to find the global optimum, here the Differential Evolution (DE) [19]. Like all evolutionary algorithms DE relies on a population X of P individuals: $X = \big\{\boldsymbol{x^{(1)}}, ..., \boldsymbol{x^{(P)}}\big\}$. Each individual is a N-components vector $\boldsymbol{x^{(i)}} = (x_1^{(i)}, ..., x_N^{(i)})$. At each iteration the population is transformed by mutation and cross-over of its individuals to form a new generation. For a given member $\boldsymbol{x}^{(i)}$ of the population of the k^{th} generation three other members of the population are selected $\boldsymbol{a} \neq \boldsymbol{b} \neq \boldsymbol{c} \neq \boldsymbol{x}^{(i)}$ and mutate according to the following formula to form a test vector $\boldsymbol{x}^{test}$:

$$x_j^{test} = a_j + F(b_j - c_j) \text{ with } j = 1, ..., N \text{ and } F \in]0; 2[\tag{21}$$

Then this vector is combined with $\boldsymbol{x}^{(i)}$ to form the candidate vector $\boldsymbol{x}^{candidate}$:

$$x_j^{candidate} = \begin{cases} x_j^{test} & \text{if } r_j \leq R \\ x_j^{(i)} & \text{if } r_j > R \end{cases} \tag{22}$$

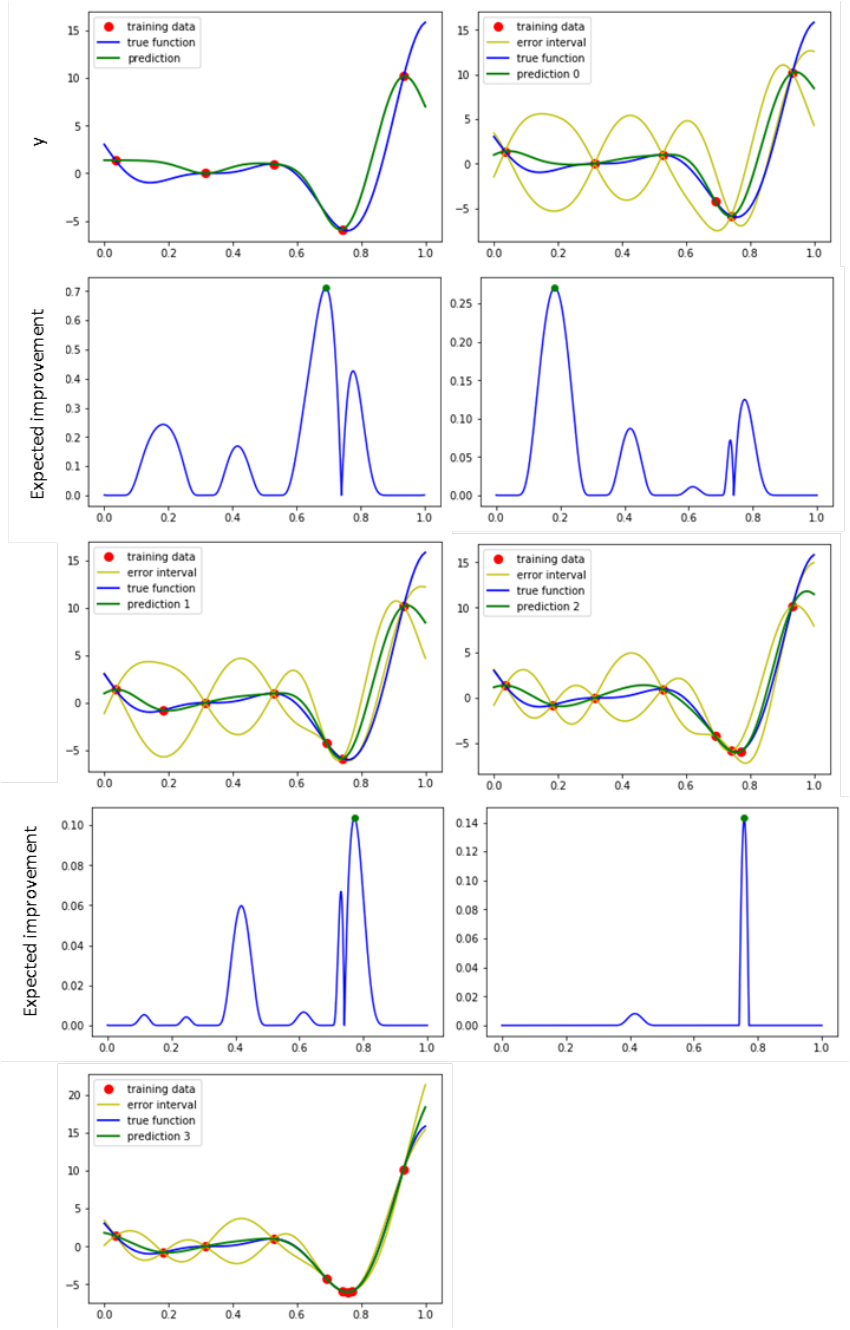

Figure 5: Illustration of Kriging-based global optimization using Expected Improvement. In four iterations the global optimum is found

In (22) $r_j's$ are randomly selected real in the interval $]0;1[$ and $R \in]0;1[$ is the recombination factor fixed by the user, here it is set to 0.6.

Then the vector in the next generation will be $\boldsymbol{x}^{candidate}$ if it improves the objective function with respect to $\boldsymbol{x}^{(i)}$ otherwise $\boldsymbol{x}^{(i)}$ is maintained in the population. The operation is reproduce for every individuals and the generations are iterated until the maximum number of iterations is reached or there is no more significant difference within the population. This algorithm can be generalized for multi-objectives optimization [20] but as it was not implemented it was decided to use an in-house tool that already had a multi-disciplinary capability using another method. This method relies on the following steps: first the anchor points are searched: these points correspond to the optimum of each objective without taking into account the others. From those

point new points are selected on the tangent plan to the Pareto set (in the design space). These points are not Pareto optimum but are used as starting point to find the nearest point on the Pareto front. This is done using a steepest descent algorithm or a quasi-Newton descent. That is to find a direction d that improves both objectives f^i:

$$d \cdot \nabla f^i \leq 0 \; \forall i \tag{23}$$

Therefore the problem to be solved is:

$$\min_d \max_i d \cdot \nabla f^i \tag{24}$$

For quasi-Newton method the Hessians of the objectives are taken into account:

$$\min_d \max_i (d \cdot \nabla f^i + 0.5[d \cdot H^i \cdot d]) \tag{25}$$

The process to find the Pareto front is illustrated on Figure 6. The black points are the two anchor points and the blue points correspond sub-optimal designs selected on the tangent plan to the Pareto set in the vicinity of an optimal design. This point is then used as starting location to find the nearest optimal (red point) configuration with descent algorithm. On the figure the Utopia and the Nadir points are also represented they correspond to the hypothetical point that respectively minimize and maximize both objectives simultaneously.

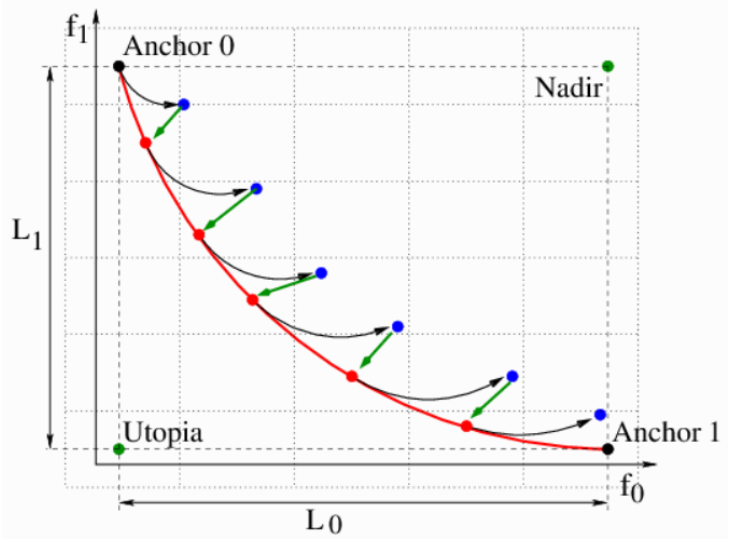

Figure 6: Multi-objective optimization Pareto front discovery strategy, [21]

3 MODELS AND PROBLEM DESCRIPTION

3.1 XRF1 Generic Model

As mentioned in the introduction the Airbus generic aircraft model XRF1 is considered for this study. XRF1 is an Airbus provided industrial standard multi-disciplinary research testcase representing a typical configuration for a long range wide body aircraft. The design point flying conditions: Mach, Altitude, Lift Coefficient, will be referred in the rest of the document as M_{cruise}, Alt_{cruise} and Cl_{cruise} respectively.

The baseline configuration of the XRF1 model does not have winglets (Fig. 7), this configuration will be the reference for the evaluation of the benefits unless an other reference is explicitly introduced.

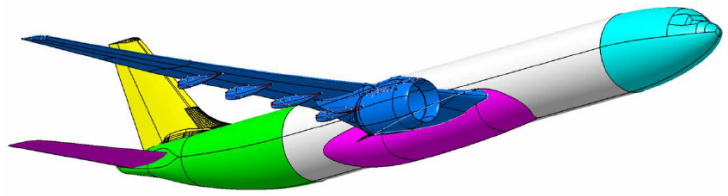

Figure 7: XRF1 baseline configuration

3.2 Aerodynamic model

To properly evaluate the aerodynamic performances and particularly the drag, high-fidelity RANS (Reynolds Average Navier-Stokes) simulations are performed with TAU solver (developed by DLR). For simplification purpose, only the right wing of the aircraft is studied, the additional drag from the tail plane stabilizer is neglected when comparing two configurations equipped with winglets. In the same way the drag and lift from the fuselage are supposed to be constant and a weight is applied to the total lift and drag coefficients to account for these contributions.

For the rest of this study and for each flight condition the simulations are performed targeting the lift coefficient corresponding to the analyzed mass cases.

The fluid domain is an hemisphere whose radius equals 45 times the wing root chord and is composed of around 5 millions nodes (Fig. 8) arranged in an unstructured grid.

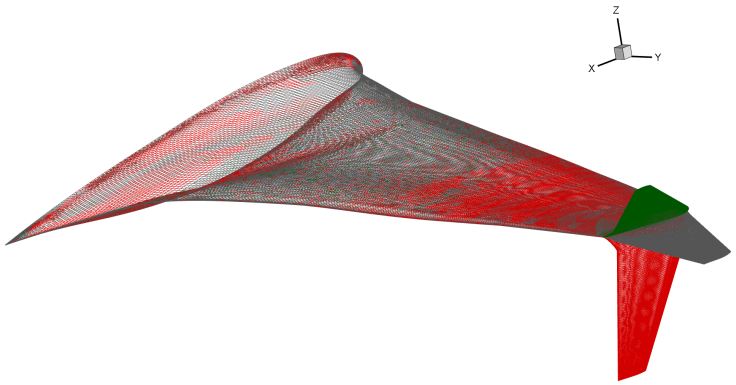

Figure 8: CFD surface mesh of the wing for different winglet geometries resulting from mesh deformation.

The flow at the surface of the wing is considered fully turbulent and the boundary layer is sufficiently refined to assure a dimensionless wall distance $y^+ < 1$ everywhere on the surface.

The second order $k-\omega$ Menter SST (Shear-Stress Transport) turbulence model is applied.
Tens of meshes will be necessary to evaluate the points of the sampling plan. As this is a fastidious task it was decided to mesh a limited number of configurations and to use a mesh deformation tool to deformed these reference meshes in order to generate the others. The cells of the mesh will be mainly deformed when the winglet cant angle will vary between two different geometries, therefore, we used five reference meshes with different cant angles while the other geometric parameters are fixed to their mid-range values.

3.3 Structural model

Wing deformations under the aerodynamic loading must be correctly computed. Therefore, a Global Finite Element model (GFEM) of the aircraft with 350 000 degrees of freedom is used (Figure 9). The aircraft is equipped with carbon fiber composite wings and fuselage modelled by 2D and 1D elements for skins and stringers(/frames) respectively. For the study, the winglets are considered as infinitely rigid and are represented in the model by a mass node rigidly linked to the main wing structure. The mass of the winglet account not only for the structural mass of the device but also for an estimated weight of the actuation system. The structural solver used is MSC-NASTRAN.

Figure 9: Global Finite Element model of XRF1.

3.4 Aeroelastic coupling

Performances and displacements can only be representative if the static aeroelastic solution is computed. Therefore the CFD and CSM solvers must be coupled in order to transfer the aerodynamic forces to the structure and resulting structural displacements to the fluid mesh. Therefore, the six degrees of freedom (DoF) of the FEM nodes must be transferred to the three DoF of the CFD surface mesh. Different interpolations methods exist to ensure this transfer, those presented hereafter were developed for FlowSimulator, the flow simulations environment used at Airbus, and exposed in the reference article [22,23]. In the present study, only two methods are used and will be explained more in details.
The first one is the "Rigid body" interpolation. This method is used when only one structural point (a mass nodes) is used to model a component, that is the case for example when engines are simplified to a massic nodes or in our case for the winglets which are modelled with only one structural node. If $x_{fem} = (x_{fem}^{(1)}, x_{fem}^{(2)}, x_{fem}^{(3)})$ is the structural node, with the associated translations (DoF 1 to 3) and rotations (DoF 4 to 6) displacements $\boldsymbol{t} = (t^{(1)}, t^{(2)}, t^{(3)}, t^{(4)}, t^{(5)}, t^{(6)})$, the CFD displacements $\boldsymbol{t_{cfd,i}}$ of node x_{cfd} are rigidly interpolated from $\boldsymbol{t}$ using the rigid inter-

polation matrix $M_{rigid,i}$:

$$M_{rigid,i} = \begin{bmatrix} 1 & 0 & 0 & 0 & dz_i & -dy_i \\ 0 & 1 & 0 & -dz_i & 0 & -dx_i \\ 0 & 0 & 1 & dy_i & -dx_i & 0 \end{bmatrix} \tag{26}$$

In the previous equation dx_i, dy_i and dz_i are equal to:

$$\begin{aligned} dx_i &= x^{(1)}_{cfd,i} - x(1)_{fem} \\ dy_i &= x^{(2)}_{cfd,i} - x(2)_{fem} \\ dz_i &= x^{(3)}_{cfd,i} - x(3)_{fem} \end{aligned} \tag{27}$$

Then the translation displacements of the CFD nodes are computed using the following matrix operation:

$$t_{cfd,i} = M_{rigid,i} \cdot \boldsymbol{t} \tag{28}$$

The second one is the "Beam coupling" interpolation. It is suited for elements whose structural nodes are aligned. In our case the mass nodes of the wing were used. Let $\boldsymbol{X_{fem}} = \{x_{fem,1}, ..., x_{fem,n}\}$ be the aligned n structural nodes, $\boldsymbol{T} = [t_1, ..., t_n]$ the matrix of the structural translations(DoF from 1 to 3) and rotations (DoF from 4 to 6), $t_i = (t_i^{(1)}, t_i^{(2)}, t_i^{(3)}, t_i^{(4)}, t_i^{(5)}, t_i^{(6)})$, and $\boldsymbol{X_{cfd}} = \{x_{cfd,1}, ..., x_{cfd,m}\}$ the $m >> n$ CDF mesh nodes. Two structural nodes, usually the first x_{ref1} and the last x_{ref2} of the beam are used to form the reference "beam", the other FEM and the CFD nodes are perpendicularly projected on the reference beam:

$$\begin{aligned} &x_{proj-fem,i} = x_{ref1} + (x_{ref2} - x_{ref1})\eta_{fem,i} \\ &x_{proj-cfd,i} = x_{ref1} + (x_{ref2} - x_{ref1})\eta_{cfd,i} \\ &\text{with } \eta \in \mathrm{R} \end{aligned} \tag{29}$$

Then the displacements $t_{proj,i}$ of $x_{proj-fem,i}$ on the beam are computed using the interpolations matrix $M_{int,i}$:

$$M_{int,i} = \begin{bmatrix} 1 & 0 & 0 & 0 & dz_i & -dy_i \\ 0 & 1 & 0 & -dz_i & 0 & -dx_i \\ 0 & 0 & 1 & dy_i & -dx_i & 0 \\ 0 & 0 & 0 & 1 & 0 & 0 \\ 0 & 0 & 0 & 0 & 1 & 0 \\ 0 & 0 & 0 & 0 & 0 & 1 \end{bmatrix} \tag{30}$$

In the previous equation dx_i, dy_i and dz_i are equal to:

$$\begin{aligned} dx_i &= x^{(1)}_{proj-fem,i} - x^{(1)}_{proj-fem,i} \\ dy_i &= x^{(2)}_{proj-fem,i} - x^{(2)}_{proj-fem,i} \\ dz_i &= x^{(3)}_{proj-fem,i} - x^{(3)}_{proj-fem,i} \end{aligned} \tag{31}$$

Therefore:

$$t_{proj,i} = M_{int,i} \cdot t_i \tag{32}$$

The displacements of the projected CFD nodes on the beam are then computed by linear interpolation of the displacements of the 2 nearest FEM projected nodes:

$$t_{proj-cfd,i} = t_{proj,j} + \frac{t_{proj,j+1} - t_{proj,j}}{\eta_{fem,j+1} - \eta_{fem,j}} \times (\eta_{cfd,i} - \eta_{fem,j}) \tag{33}$$

The matrix $M_{rigid,i}$ is then used to computed the CFD nodes displacements from those of their projection on the beam. the only difference with respect to (26) is that dx_i, dy_i and dz_i are changed to:

$$\begin{aligned} dx_i &= x^{(1)}_{cfd,i} - x^{(1)}_{proj-cfd,i} \\ dy_i &= x^{(2)}_{cfd,i} - x^{(2)}_{proj-cfd,i} \\ dz_i &= x^{(3)}_{cfd,i} - x^{(3)}_{proj-cfd,i} \end{aligned} \tag{34}$$

Finally the CFD translation displacements are computed by rigid interpolation of the displacements of their projections on the beam:

$$t_{cfd,i} = M_{rigid,i} \cdot t_{proj-cfd,i} \tag{35}$$

The two couplings methods are illustrated on Figure 10. The wing CFD and FEM nodes are coupled with "Beam" interpolation methods, while winglet presents a rigid body coupling.

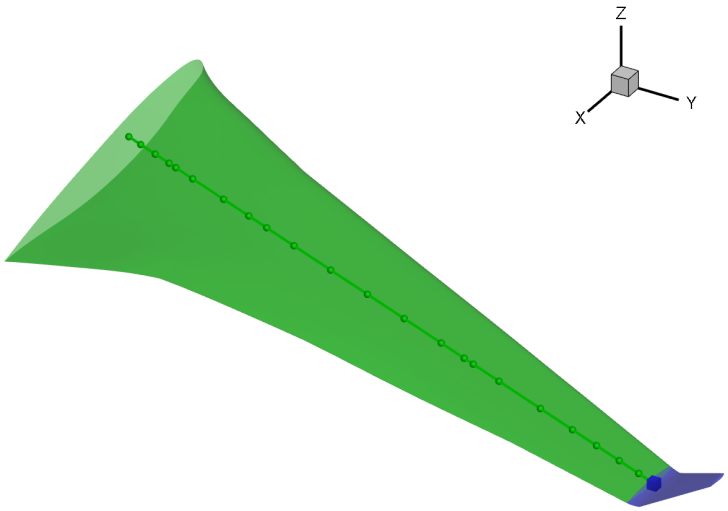

Figure 10: Example of beam and rigid body couplings on the XRF1 wing – Green dots represent the structural nodes of the wing, green surface is the CFD surface to be coupled with – Blue cube is the winglet structural nodes, blue surface is the CFD surface to be rigidly coupled with.

Regarding force transfer, the inverse of the interpolation matrix M_{all} that gather all the $M_{int,i}$ matrices can be used to computed the forces and moments F_{fem} to be applied on the structured from the aerodynamic forces F_{cfd}:

$$F_{fem} = M^t_{all} \cdot F_{cfd} \tag{36}$$

This method ensures the conservation of virtual work. Another method consists in computing the structural forces and moments on a given FEM node from those of the nearest CFD nodes. This method is refereed as "Nearest Neighbour" transfer. It ensures the conservation of the forces and moments. For a given structural point all $x_{fem,i}$ the CFD nodes whose the closest structural point is $x_{fem,i}$ are gathered in the set NN_i then the forces and moments ($L^f_{fem,i}$ and $L^m_{fem,i}$ respectively) are computed at $x_{fem,i}$ location from the aerodynamic forces $L^f_{cfd,j}$:

$$\begin{aligned} L^f_{fem,i} &= \sum_{j \in NN_i} L^f_{cfd,j} \\ L^m_{fem,i} &= \sum_{j \in NN_i} (x_{cfd,j} - x_{fem,i}) \times L^f_{cfd,j} \end{aligned} \tag{37}$$

Once the surface displacements are computed, the volume mesh must be deformed. Radial Basis Functions are used to interpolate the surface displacements. The centers of the RBF are the surface mesh points and the displacements of the volume node x_{vol} is given by:

$$t_{vol}(x) = \sum_{i=1}^{m} \alpha_i \phi(||x - x_{cfd,i}||) \tag{38}$$

The coefficients α are computed using the displacement at the basis points: $t_{vol}(x_{cfd,i}) = t_{cfd,i}$. The radial basis function used is the Wendland's C^0 function:

$$\phi(||x||) = \begin{cases} (r - ||x||)^2 & : ||x|| \leq r \\ 0 & : ||x|| > r \end{cases} \tag{39}$$

The parameter $r \in \mathrm{R}$ is selected by the user in our case the value 10 gives good results. The mesh deformation is not propagated to the entire volumic cells only the nodes at a certain distance $D_{zero-weight}$ of the surface are affected. The deformation of the surface is fully applied to the volume nodes in a radius of $D_{full-weight}$ then the influence of the surface deformation is gradually decrease between $D_{full-weight}$ and $D_{zero-weight}$.

3.5 Optimization problem description

The aim of this study is to evaluate the efficiency of an active winglet to optimize the aircraft performances. To do so, first a winglet will be optimized for the XRF1 at cruise conditions. Then the cant angle of the optimal design will be change to minimize the fuel consumption of the aircraft along a mission, the other design variables are frozen to their optimal value. The Figure 11 shows the optimization process.

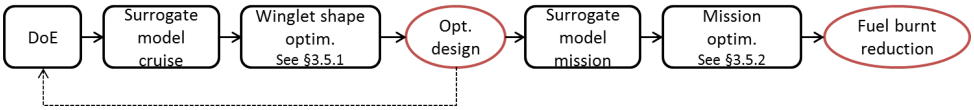

Figure 11: Overview of the optimization process

3.5.1 Winglet geometry optimization problem

As mentioned above, the XRF1 baseline wing is not equipped with winglets, thus the first part of the study was dedicated to the planform optimization of a winglet for this configuration, taking into account both aerodynamic performances and impact on the structure. The optimization is performed for the design point flying conditions as it would be for a classical design approach. The aircraft weight is fixed to a value representative of an average mid-cruise weight and the targeted lift coefficient (Cl_{cruise}) is computed in consequence. The design variables are the winglet cant (Ca), sweep (Sw) and tip twist (Tw) angles and the span (S) and tip chord (C) lengths. Figure 12 shows how the winglet shape is modified as design variables change. At this stage, an important remark should be made: the profiles of the winglet are not optimized, they are generated from the last wing rib profile and scaled this is an acceptable approximation for the targeted goals of the study.
The limits of the design space are detailed on table 1.

The optimization of the winglet must target the best aerodynamic performance that is the lowest possible drag (as the Cl is fixed) but it also should take into account the impact on the structure. Indeed, this study takes place in a retrofit context that prevents large modification of

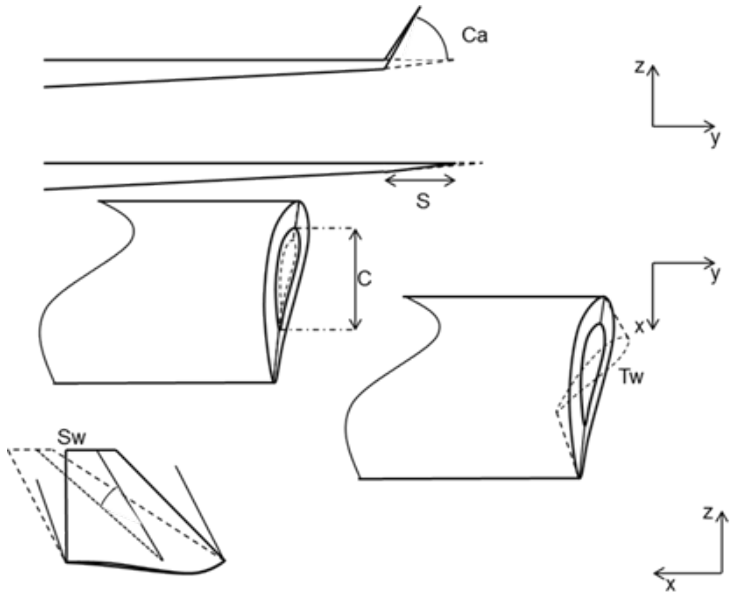

Figure 12: Design variable description, Dot line represents the shape alteration as the design variables changes – X = aircraft longitudinal axis, Y = aircraft lateral axis – Z = vertical axis (positive up)

Table 1: Design space limits

Design variable	Range
Cant angle (deg)	[-90 ; 90]
Sweep angle (deg)	[30 ; 60]
Tip Twist angle (deg)	[-5 ; 5]
Span (m)	[2.0 ; 5.0]
Tip Chord (m)	[0.4 ; 2.3]

the structure. As a results the optimal solution is a trade-off between drag and structural impact minimization. As stresses are not computed, the impact on the structure will be evaluated through the value of the wing root bending moment (WRBM). Besides, as the objective of the active winglet is to control wing shape, an additional constraint is added: a given winglet configuration must be able to alter the wing tip twist (junction wing/winglet) by an amount greater than a threshold $\Delta Twist_{target}$ when the can angle of the configuration varies from $-90\,\mathrm{deg}$ to $+90\,\mathrm{deg}$. The optimization problem is then formalized as follow:

$$\begin{aligned} \min_{\boldsymbol{x}} \quad & F(\boldsymbol{x}) = (Cd(\boldsymbol{x}), WRBM(\boldsymbol{x})) \\ \text{with} \quad & \boldsymbol{x} = [Ca, Sw, Tw, S, C] \\ \text{s.t.} \quad & \begin{cases} Cl = Cl_{cruise} \\ M = M_{cruise} \\ Alt = Alt_{cruise} \\ |\Delta Twist| \geq |\Delta Twist_{target}| \end{cases} \end{aligned} \tag{40}$$

3.5.2 Mission optimization problem

For this second step the winglet shape is frozen in the optimal planform determined in the previous part. Only the cant angle is now authorized to change during the optimization process.The

mission is divided into several segments, for each segment i the fuel burnt is minimized and the total fuel consumption is computed by integration. This optimization problem is formalized as follow:

$$\begin{aligned} \min_{\boldsymbol{x}} \quad & Fuel_i \\ \text{with} \quad & \boldsymbol{x} = [Ca_i] \\ \text{s.t.} \quad & \begin{cases} Cl = Cl_i \\ M = M_i \\ Alt = Alt_i \end{cases} \end{aligned} \tag{41}$$

Mission performance assessment methodology

In this study the performance assessment is performed for a given range and a given mission profile (Speeds and Altitudes). The cruise is subdivided in N segments of length $\frac{Range_{cruise}}{N}$ while the climb is separated in segments of equals vertical distance dh. Figure 13 illustrates the mission profile segmentation. In this study, the descent is not taken into account as it represents a negligible part of the flight and of the fuel consumption (around 1%) for a long-range aircraft.

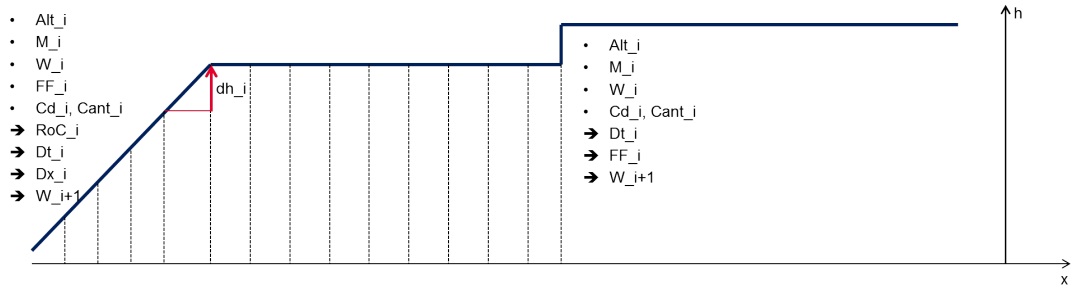

Figure 13: Mission segmentation - dot = inputs, arrows = output of the mission computation

As for the winglet shape optimization a CFD/CSM computations database is generated taking into account the optimal design resulting from the shape optimization as described in previous paragraph 3.5.1 with a variable cant angle, this model is used to evaluate the drag D_i for each segment. Besides a generic engine model, representative of a long-range aircraft engine is used to compute the fuel flow and the thrust for the different flight phase.

Climb

For the climb part, the rating of the engine is fixed to the max-climb condition that is the fuel-flow FF_i and the thrust Th_i are fixed for each segment. The initial aircraft weight of a segment equals the final weight W_i of the previous one or the take-off weight for the first segment. Here, for simplicity, the acceleration phases are not considered and the speed is constant on each segment, then the equilibrium of the aircraft is given by:

$$L_i = W_i \times \cos(\gamma) \approx W_i \tag{42}$$

$$Th_i \times \cos(\gamma) - D_i \times \cos(\gamma) = L_i \times \sin(\gamma) \leftrightarrow \sin(\gamma) = \frac{Th_i - D_i}{L_i} \tag{43}$$

In the previous equations γ is the aerodynamic slope. The rate of climb RoC_i is computed from the True Air Speed (TAS) V_i:

$$RoC_i = V_i \times \sin(\gamma) = V_i \times \frac{Th_i - D_i}{W_i} \tag{44}$$

Then the time dt_i spent on the segment is evaluated by taking into account the vertical distance to be covered:

$$dt_i = \frac{dh}{RoC_i} \tag{45}$$

The fuel consumption on the segment can be deduced from the fuel flow value and the new weight computed:

$$W_{i+1} = W_i - FF_i \times dt_i \tag{46}$$

Finally the ground distance dx_i is computed:

$$dx_i = \sqrt{\left(\frac{dh \times V_i}{RoC_i}\right)^2 - dh^2} \tag{47}$$

The mission is performed according to a predefined climb speed profile: below 10,000ft the Calibrated Air Speed (CAS) is limited to 250kt, between 10,000ft and the crossover altitude the CAS is fixed to 300kt and above the crossover altitude the climb is continued at Mach 0.78 until the first cruise altitude is reached. The atmospheric conditions used to computed the TAS are consistent with the ICAO Standart Atmosphere (ISA). At the end of the climb phase, the remaining cruise range ($Range_{cruise}$) is computed.

Cruise

Several cruise altitudes can be defined *a priori* and a portion of the cruise range is affected to each of them. The portions of constant altitude are then subdivided in segments, for each segment the aircraft equilibrium gives:

$$\begin{aligned} L_i &= W_i \\ D_i &= Th_i \end{aligned} \tag{48}$$

The drag is computed from surrogate models whose inputs are the altitude, the speed (Mach), the aircraft weight and the winglet cant angle. The fuel flow is derived from the engine model:

$$FF_i = f(Th_i, Alt_i, M_i) \tag{49}$$

The time spent on the segment i is computed from the TAS:

$$dt_i = \frac{dx_i}{V_i} \tag{50}$$

The fuel consumption and initial weight for the next segment is then deduced:

$$W_{i+1} = W_i - dt_i \times FF_i \tag{51}$$

4 RESULTS

4.1 Surrogate building and validation

As explained in the theoretical part, surrogate models were built to replace the CFD/CSM computations in the optimization process. These models rely on a database of around 500 converged CFD/CSM computations for different winglet configurations in cruise conditions. Each computation was launched on 96 processors and took approximately six hours, the full data-base was generated in a bit less than one day (22 hours), then the exploitation of the model is very fast: up to five minutes for multi-objective optimization. Surrogate models for drag, wing twist and

wing root bending moment were built. However, to gain confidence in the results provided by the surrogate-based optimization the models must be precise enough. The quality of the surrogates was evaluated through the cross-validation process as described in paragraph 2. The initial DoE is divided in ten subsets, among those subsets five are selected to perform cross-validation and the metrics (RMSE and R^2) are computed as the means over those five subsets. The results of the cross-validation for each model are presented on Table 2 and show the very good quality of the models, with low RMSE and high values of the coefficient R^2. The mean error on drag does not exceed 0.15 drag counts which is satisfactory since a precision of 1 drag-count is targeted. Regarding wing twist and wing root bending moment the results are even better with $R^2 > 0.99$ and very low RMSE: for WRBM the error represents 0.05% of the WRBM of the baseline wing and for twist the error falls to 0.01% of the baseline wing twist value.

Figure 14 shows the drag model evolution as function of winglet cant angle and winglet span

Table 2: Surrogate models quality assessment results from cross-validation – RMSE are in the unit of the models: Drag count for Drag, Degree for Twist and N.m for WRBM.

Model	RMSE	R^2
Drag	$1.47e^{-05} D.C$	0.989
Twist	$2.94e^{-04}$ deg	0.994
WRBM	$4537 N.m$	0.993

while the other variables are fixed to their mid-range values.

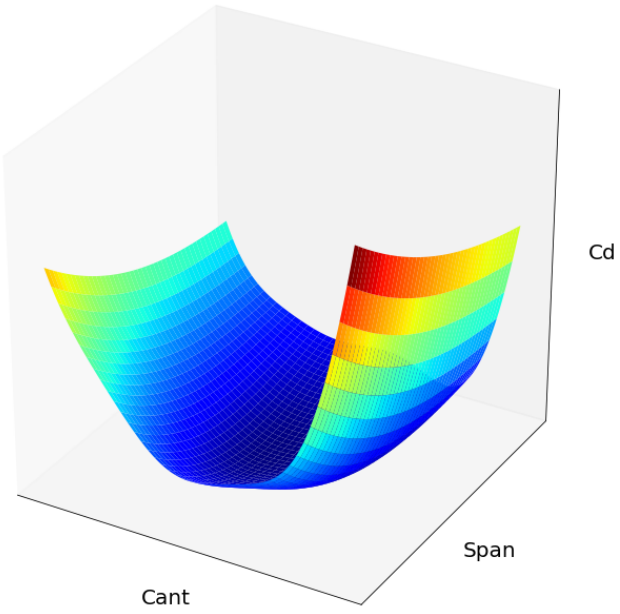

Figure 14: Drag coefficient surrogate model evolution as function of winglet cant and span – other variables fixes to mid-range values

4.2 Results and selection of the optimal shape

The surrogate models were used to perform the multi-objective optimization targeting to minimize the drag in cruise conditions while minimizing the impact on loads assessed by the value

of the wing root bending moment. Figure 15 shows the Pareto front resulting from the optimization, it highlights the antagonism between the two objectives. The blue circle indicates the selected configuration. This winglet enables a reduction of 4% of the total drag with respect to the baseline while limiting the increase of wing root bending moment to an acceptable 2%. This increase may necessitate structural reinforcements, but sizing margins can cover it. The characteristics of the optimal design are detailed on Table 3. This optimal configuration results from a surrogate prediction and must be validated using the "true" function, computation shows a relative difference between the prediction and the true function of 0.025% demonstrating again the precision of the surrogate.

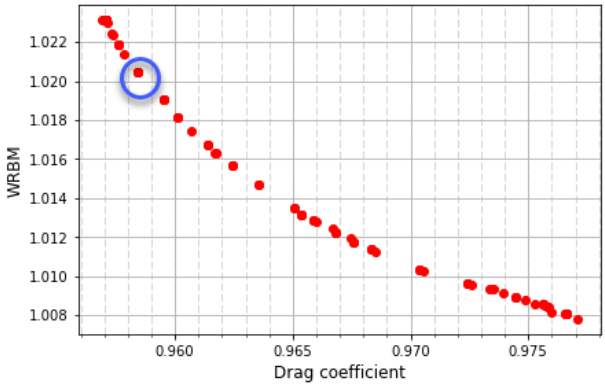

Figure 15: Pareto front of the multi-objective optimization - Relative Drag Coefficient and WRBM as objecives

Table 3: Design space limits

Design variable	Optimal value
Cant angle (deg)	-4.1
Sweep angle (deg)	30
Tip Twist angle (deg)	4.4
Span (m)	4.0
Tip Chord (m)	0.8

The optimal design presents a slightly negative cant angle, Table 3. It was demonstrated that such winglets better perform than upward ones as the tip vortex core is rejected farther from the symmetric plane increasing the apparent span. Besides due to the wing dihedral angle δ the maximum projected span is reached when $Ca = -\delta$ [24]. Figure 14 shows that the drag raises quickly when the cant angle increases. This is attributed to the reinforcement of the shock in the region of the junction between the wing and the winglet. The region acts like a corner that locally accelerates the flow and reinforces the shock. Besides the possible interaction between the shock on the winglet and the shock on the wing strengthened the latter. In certain cases, the shock is so strong that flow separation may occur that would increase the drag even more. Considering loads, downward winglets are also advantageous: the wing root bending moment due to the lateral aerodynamic force (in Y direction) acting on the winglet – when this one is not horizontal – is more important for upward configurations due to an higher lever arm. All this arguments advocate for slithly downward winglets as optimal solutions.

4.3 Results mission optimization

4.3.1 Rigid computation

Many studies dealing with active winglets assess the performances of the device in cruise conditions for the undeformed flight shape [12, 13] (i.e. not considering fluid/structure interactions). Besides, the baseline is not necessarily optimized. In the present document, the first mission optimization was performed for a constant cruise altitude (Alt_{cruise}). To assess the impact of the choice of the baseline configuration a first analysis will be performed with a non-optimized cant angle for example $50\,\mathrm{deg}$, as in [12], while the other shape parameters (span, chord, twist, sweep) are those detailed in table 3. The mission range is fixed to 4,000nm, which representative of a long-range flight.

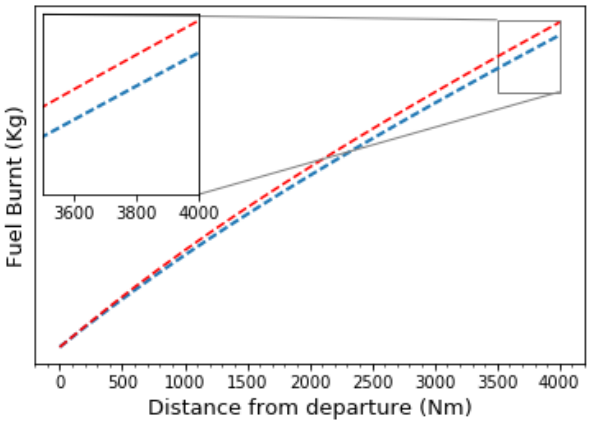

Figure 16: Fuel consumption along the mission. Baseline with non-optimal cant angle: red line – Active winglet configuration: blue line

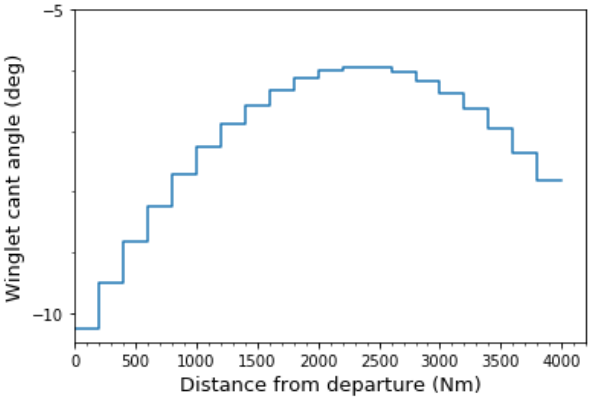

Figure 17: Optimal winglet deflections along the mission

The baseline is compared to the active winglet whose cant angle is free to move from $-90\,\mathrm{deg}$ to $+90\,\mathrm{deg}$. Figure 16 shows the evolution of the fuel burnt mass during the flight, noticeable benefits from the active winglet are highlighted. A relative gains of 4% is achieved on the final weight for the active winglet configuration. The winglet deflection during the flight is shown on Figure 17: the actuation range is around $4\,\mathrm{deg}$ which is rather low and advocates for a fixed device set at the average deflection value. The comparison of the drag coefficients along the flight demonstrates that the active winglet enable to reduce the drag whatever the aircraft weight (fig. 18), the relative gains range from 4.75% to 2.75%.
The case with the optimal design as detailed in Table 3 was also analyzed, this design was ob-

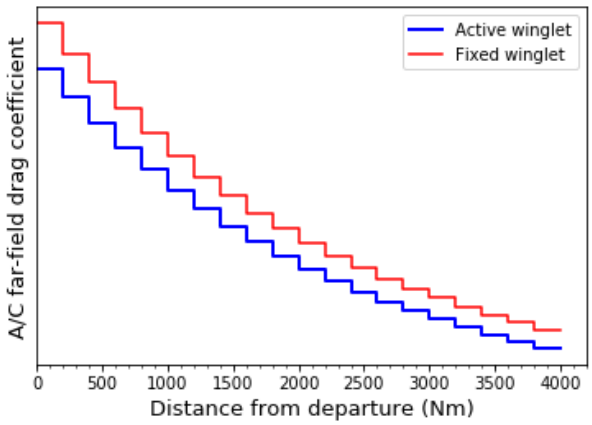

Figure 18: Drag Coefficient evolution along the flight.Baseline with non-optimal cant angle: red line – Active winglet configuration: blue line

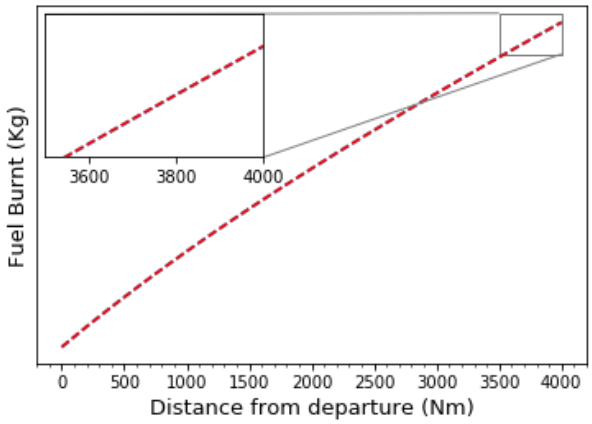

Figure 19: Fuel consumption along the mission. Baseline with optimal cant angle: red line – Active winglet configuration: blue line

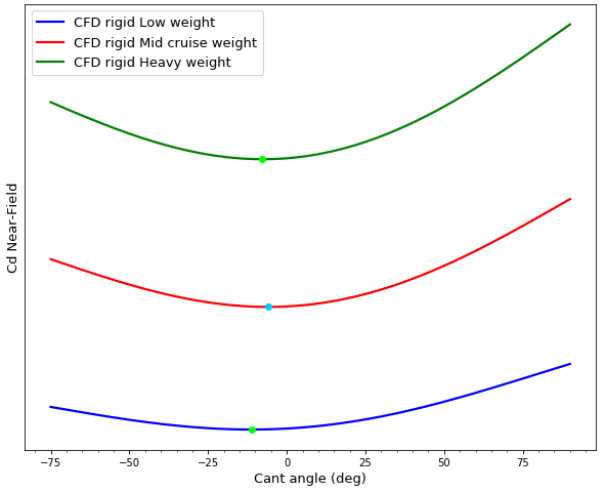

Figure 20: Drag coefficient evolution as function of the winglet cant angle for different mass cases from surrogate model. Dots represent the minimum drag configuration

tained for flexible computations therefore it may not correspond to the exact optimum for rigid case but may be in the neighbourhood of the latter. The results for the active winglet are the same as the optimization is not affected by the baseline selection, however the benefits are drastically lowered as anticipated. As shown on Figure 19, the fixed and the active configuration are

almost identical in term of fuel consumption.
The drag evolution as function of the cant angle is plotted on Figure 20 (extracted from the surrogate model)and shows a relatively flat region around the optimal cant angle explaining the marginal gains when the optimal design is used as a reference and also the limited actuation range.
These results highlight that the selection of the baseline is determinant and to properly assess the efficiency of the active device an optimized fixed configuration should be used as a reference.

4.3.2 Flexible computations

As aircraft are flexible it is suited to take into account this parameter in the optimization of the mission performances. Indeed the winglet setting has an impact on the lift distribution and as a result on the wing deformation, particularly the twist of the wing will be affected. New surrogate models based on CFD/CSM computation were built to compute the drag on the whole flight domain. The same optimizations as those described in the previous paragraph 4.3.1 were performed. Results are presented on Figure 21 to Figure 23 for the non-optimized baseline

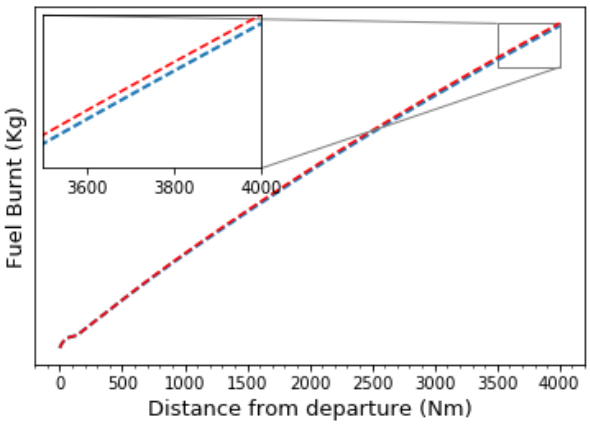

Figure 21: Fuel consumption along the mission for flexible cases. Baseline with non-optimal cant angle: red line – Active winglet configuration: blue line

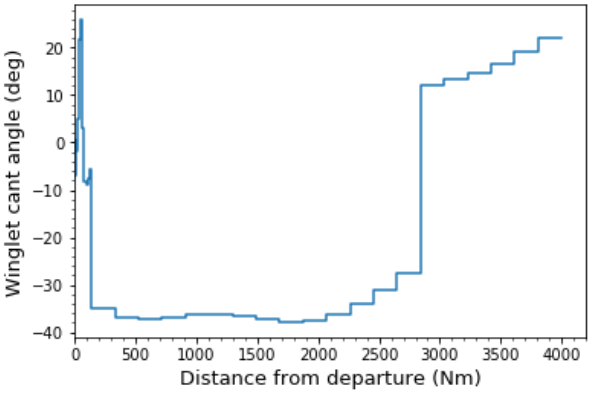

Figure 22: Optimal winglet deflections along the mission for flexible case

case. Fuel consumption benefits are still observable when the winglet is actuated. However, only 1% of gains are reach with respect to the baseline while 4% were reached for the rigid case. The winglet actuation range is drastically increased to $50\,\mathrm{deg}$ but the effect is limited. The step on the winglet deflection graph occurs when two successive weights surround the design weight. As the weights are slightly different the deflections are not identical. Besides as shown

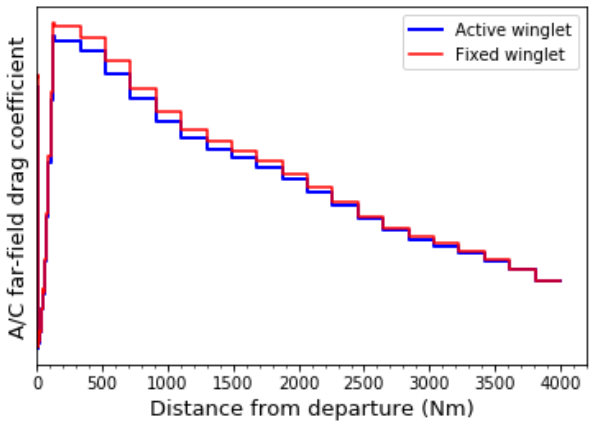

Figure 23: Drag Coefficient evolution along the flight for flexible cases. Baseline with non-optimal cant angle: red line – Active winglet configuration: blue line

on 26 there is very few drag evolution between $-40\,\mathrm{deg}$ and $25\,\mathrm{deg}$, the step may be consider as a computation artifact and a continuous curve would have give almost the same result. The relative drag difference ranges from -1.75% to 0% when the weight decreases (fig. 23). When the optimal design is considered the gains are even more reduced and barely reach 0.1% (fig. 24), as for the rigid case. The impact of the winglet deflection on the wing twist are highlighted on Figure 25. At the beginning of the flight, for heavy mass cases i.e. high Cl, the winglet is deflected downward with respect to the optimal configuration, the consequence is an augmentation of the local angles of attack and a slightly more external loading. The two curves cross when the aircraft weight is near from the design weight (i.e. $Cl = Cl_{cruise}$). After that point, the consequence of the actuation of the winglet is a lower wing twist to maintain, as far as possible, on optimal loading.
The drag evolution as function of the winglet can angle for different mass cases (fig. 26) highlights that the introduction of the flexibility tends to flatten the drag curve and reduce the sensitivity of the drag coefficient to the winglet cant angle. As a results the gains are negligible.

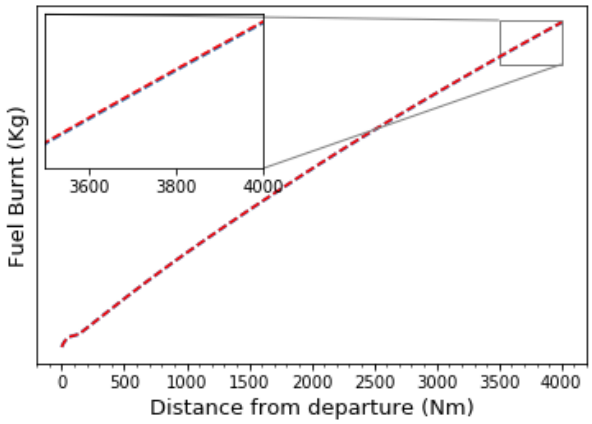

Figure 24: Fuel consumption along the mission for flexible cases. Baseline with optimal cant angle: red line – Active winglet configuration: blue line

To understand the difference between the flexible and the rigid cases. One should consider the induced drag formula:

$$Cd_i = \frac{Cl^2}{\pi \times AR_{proj} \times e} \tag{52}$$

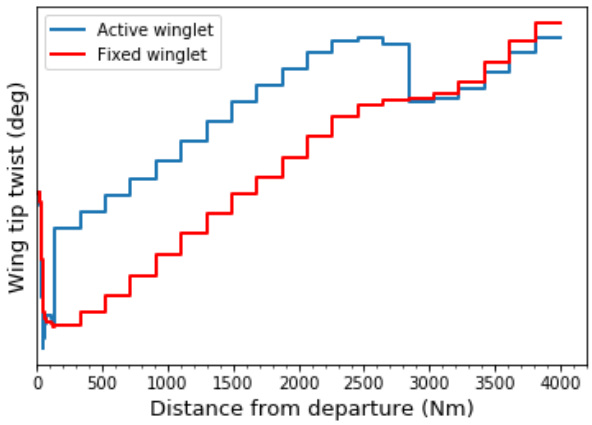

Figure 25: Wing Twist variation during the flight. Baseline with optimal cant angle: red line – Active winglet configuration: blue line

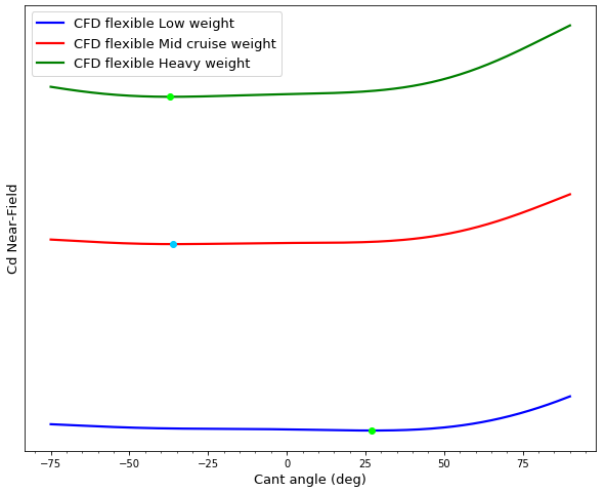

Figure 26: Drag coefficient evolution as function of the winglet cant angle for different mass cases from surrogate model. Dots represent the minimum drag configuration

In (52) the term AR_{proj} stands for the projected Aspect Ratio and e is the Aerodynamic efficiency factor that is 1 for the elliptic lift distribution. In the rigid case the predominant term in the equation is the projected Aspect Ratio, as a results the drag will be optimal for the maximal AR_{proj} i.e. for winglet cant angle slightly negative (taking the wing dihedral angle into account). Indeed in this case the aerodynamic efficiency factor will be directly linked to the wing aspect ratio as flat configurations will lead to more external lift distribution closer to the ideal elliptic case, the local angles of attack remaining unchanged. For flexible cases, the wing will be deformed under the aerodynamic loading, this deformation will modify the local angles of attack and as a results will affect the lift distribution. As for rigid case the winglet deflection will also impact the projected wing aspect ratio. Unfortunately, unlike rigid cases, these effects are not in phase and may act in opposite directions: when the winglet is flat the wing twist will be lower than for higher cant angle values, then the local angle of attack will be reduced and the aerodynamic efficiency factor less advantageous. When the absolute value of winglet cant angle increases it exists a combination of AR_{proj} and e that gives an optimal configuration. Above this value both parameters acts in the same direction but the sensitivity to induced drag is negative. Figure 27 illustrates what have been explained above, the spanwise lift coefficient distribution of two configurations of winglets ($75\,\mathrm{deg}$ and $0\,\mathrm{deg}$) are plotted for rigid and flexible computations. It is clear that for rigid computations the flat winglet leads the more external loading

and there is a significant difference between the two configurations. For flexible computations, due to wing deformation the difference is less pronounced and concentrated near the wing tip. However, the flat winglet configuration still presents a slightly more advantageous loading (in term of aerodynamic performance). This part shows that the flexibility alters significantly the

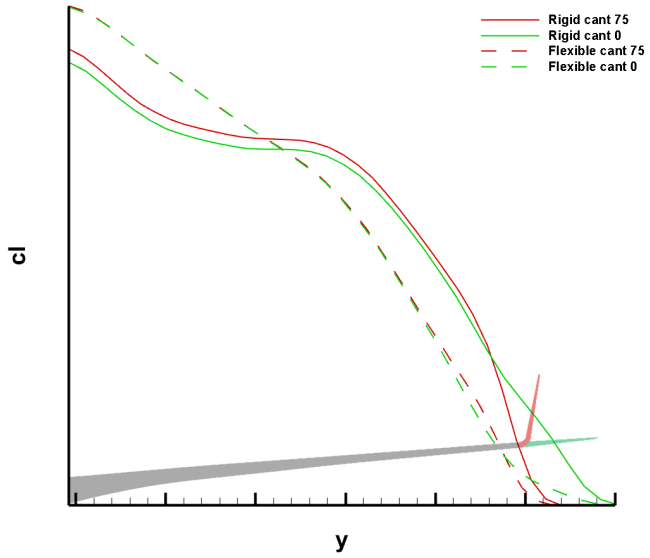

Figure 27: Illustrative spanwise lift coefficient distribution with two winglets configurations – red: 75deg, green: 0deg – For rigid (solid line) and flexible (dashed line) computations

results. Because of the wing deformation the aerodynamic efficiency coefficient and the aspect ratio are not in phase when the cant angle evolves which tends to decrease the sensitivity of the drag to the winglet position. Therefore, the efficiency of the active winglet is reduce and becomes negligible.

4.3.3 "Off-design" flexible computations

The previous statement should be slightly moderated as the computations were performed for the design point altitude. Therefore, little evolution of drag are expected when varying the winglet cant angle. Missions at different altitudes must be analyzed before any conclusion is made. Because of air traffic control limitations, weather conditions and performances, it is very unlikely that the aircraft will be operated at the design cruise altitude for the entire mission and for every flights. Besides, keeping retrofit in mind, the results show that if an aircraft was designed with a winglet a little sub-optimal e.g. $50\,\mathrm{deg}$ to respect airports constraints, the recourse to an active winglet could bring 1% of fuel savings. A computation for an "off-design" condition corresponding to the lower-bound of the cruise altitude, $Alt_{off-design} < Alt_{cruise}$, was performed. The results presented on Figure 28 demonstrate fuel saving of around 0.4% compared to the optimal baseline. This value is consistent with the expected gains when optimizing an existing wing equipped with a winglet. However, the amount a fuel saved may not be compensated by the additional costs of the actuation that are not taken into account in this, for example the hydraulic or electric system weight (except actuator), maintenance, uncertainties on the actuator weight.

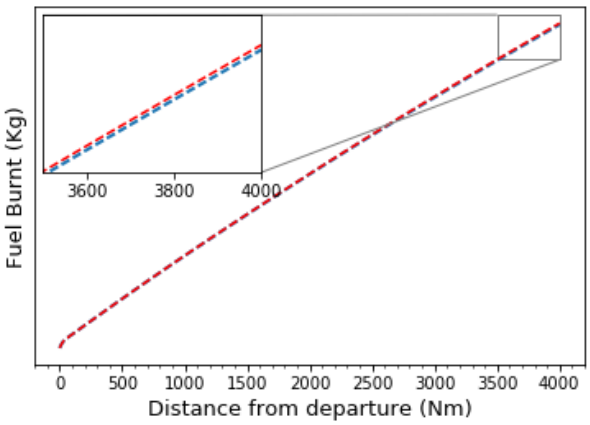

Figure 28: Fuel consumption along the mission for ”off-design” case. Baseline with optimal cant angle: red line – Active winglet configuration: blue line

5 CONCLUSION

In this paper the efficiency of an active winglet concept is evaluated using high-fidelity CFD/CSM computations. First a surrogate-based multi-objective optimization of the winglet shape is performed taking into account both aerodynamic performances and impact on loads. The designed winglet improves the performances of the baseline by 4%. Then a mission analysis was performed to optimized the winglet deflection along a representative flight. For this study, both rigid and flexible computations were realized.

It is demonstrated that the wing flexibility plays a key role in the assessment of the efficiency of such a device. It is also shown that the choice of the reference configuration is essential and an optimal design should be used to properly evaluate the additional gains due to the actuation of the devise. In the presented cases: the benefits of the active winglet fall from 4% of block fuel saving to 1% when comparing rigid and flexible cases with a non-optimal baseline configuration. The gains drop again when considering an optimal design as the baseline. Active winglets are more appealing for ”off-design” conditions, in this study a constant altitude mission performed at a lower flight level than the design point shows incremental gains of 0.4% compared to the optimal fixed design. This order of magnitude is consistent with the expectation when improving a winglet design on an aircraft already equipped with such device. Here the interest of the actuation of the winglet is limited if only the performance aspects are considered.

Future work will be dedicated to assess the impact of active winglet on loads and evaluate the loads alleviation capability of such a device. Indeed, if the winglet is able to reduce the loads for some specific points in the flight envelop additional gains would come out from a lighter structure. The impact on flutter characteristics remain to be analyzed. The concept will be tested on another aircraft wing model to check the generality of the conclusions and finally, the process will be applied on a complete aircraft (and not only considering the wing) to assess more precisely the drag from other parts of the aircraft.

6 REFERENCES

[1] Whitcomb, R. T. (1976). A design approach and selected wind-tunnel results at high subsonic speeds for wing-tip mounted winglets. Tech. Rep. TN D-8260, NASA.

[2] Moy, G., Jokisch, C. E., Good, M. S., et al. (2017). Folding wing system. The Boeing Company. US patent 2017/0349296A1.

[3] Vasista, S., Tong, L., and Wong, K. C. (2012). Realization of morphing wings: A multidisciplinary challenge. *Journal of Aircraft*, 49(1), 11–28.

[4] Barbarino, S., Bilgen, O., Ajaj, R. M., et al. (2011). A review of morphing aircraft. *Journal of Intelligent Material Systems and Structures*, 22, 823–877.

[5] Nguyen, N. and Tal, E. (2015). A multi-objective flight control approach for performance adaptive aeroelastic wing. 56th AIAA/ASCE/AHS/ASC Structures, Structural Dynamics, and Materials Conference, AIAA SciTech Forum.

[6] Nguyen, N., Kaul, U., Lebofsky, S., et al. (2015). Development of variable camber continuous trailing edge flap for performance adaptive aeroelastic wing. SAE 2015 AeroTech Congress & Exhibition.

[7] Nguyen, N., Ting, E., Chaparro, D., et al. (2017). Mutli-objective flight control for drag minimization and load alleviation of high-aspect ratio flexible wing aircraft. 58th AIAA/ASCE/AHS/ASC Structures, Structural Dynamics, and Materials Conference, AIAA SciTech Forum.

[8] FlexSys (2014). *FlexFoil by FlexSys Uses Distributed Compliance to Help Achieve Significant Fuel Savings and Noise Reduction*. Press release.

[9] Peter, F. and Stumpf, E. (2018). The development of morphing aircraft benefit assessment. *Morphing WingTechnologies*, 103–121.

[10] Concilio, A. and Lecce, L. (2018). Historical background and current scenario. *Morphing Wing Technologies*, 3–84.

[11] Barriety, B. (2004). Aircraft with active control of the warping of its wings. Airbus France. US patent 6827314B2.

[12] Cooper, J. E., Chekkal, I., Cheung, R., et al. (2015). Design of a morphing wingtip. *Journal of Aircraft*, 52(5), 1394–1403.

[13] Wang, C., Khodaparast, H., Hamed, and Friswell, I., Michael (2015). Investigating the benefits of morphing wing tip devices - a case study. International Forum on Aeroelasticity and Structural Dynamics.

[14] Quiepo, V., Nestor, Haftka, T., Raphael, Shyy, W., et al. (2005). Surrogate-based analysis and optimization. *Progress in Aerospace Sciences*, 41, 1–28.

[15] Jin, R., Chen, W., and Sudjianto, A. (2005). An efficient algorithm for construction optimal design of computer experiments. *Journal of Statistical Planning and Inference*, (134), 268–287.

[16] Krige, D. (1951). A statistical approach to some basic mine valuation problems on the witwatersrand. *Journal of the Chemical Metallurgical & Mining Society of South Africa*, 52(6), 119–139.

[17] Forrester, I., Alexander, Sobester, A., and Keane, J., Andy (2008). *Engineering Design via Surrogate Modelling - A practical Guide*. United Kingdom: Wiley & sons.

[18] Jones, R., Donald (2001). A taxonomy of global optimization methods based on response surfaces. *Journal of Global Optimization*, (21), 345–383.

[19] Storn, R. and Kenneth, P. (1997). Differential evolution – a simple and efficient heuristic for global optimization over continuous spaces. *Journal of Global Optimization*, (11), 341–359.

[20] Verstraete, T., Muller, L., and Aissa, M. H. (2018). Multidisciplinary optimization of turbomachinery components using differential evolution. In *Introduction to Optimization and Multidisciplinary Design*, von Karman Institute Lecture Series: 2018-04.

[21] Datadvance (2017). *GTopt: Multi-objective optimization*. P7 Technical reference.

[22] Stickan, B., Bleecke, H., and Schulze, S. (2013). Nastran based static cfd-csm coupling in flowsimulator. In N. Kroll, R. Radespiel, J. Burg, and K. Sorensen (Eds.), *Computational Flight Testing*, vol. 123 of *Notes on Numerical Fluid Mechanics and Multidisciplinary Design*. Springer Berlin Heidelberg, pp. 223–234.

[23] Stickan, B., Arne, R., Helm, S., et al. (2017). High-fidelity cfd-csm interaction in the industrial context. International Forum on Aeroelasticity and Structural Dynamics (IFASD).

[24] Bourdin, P. (2004). Numerical prediction of wing-tip effects on lift-induced drag. International Council of The Aeronautical Sciences.

COPYRIGHT STATEMENT